Progress in Organic Coatings 184 (2023) 107859

Contents lists available at ScienceDirect

Progress in Organic Coatings

journal homepage: www.elsevier.com/locate/porgcoat

Ultrafast synthesis of novel coal-based graphene and its anticorrosion properties of epoxy/graphene nanocomposite coatings

Yuntian Liao, Rongtao Zhu *, Wenjun Zhang, Zhuang Liu, Haiyang Zhu, Yang Sun

School of Chemical Engineering and Technology, China University of Mining and Technology, Xuzhou 221116, Jiangsu, China

ARTICLE INFO

Keywords:
Coal-based graphene
Flash Joule heating
Composite coating
Corrosion resistance
Epoxy

ABSTRACT

Graphene has a wide range of applications in anti-corrosion coatings due to its excellent barrier, shielding, and mechanical properties. However, traditional graphene synthesis methods, including the production of graphene oxide (GO) using Homer's method and then its reduction in the form of reduced graphene oxide (rGO) are time-consuming, energy-consuming, and environmentally polluting, which limits their application in anti-corrosion coatings. This study leveraged the capabilities of flash Joule heating (FJH) to synthesize flash coal-based graphene (FCBG) from Taixi anthracite (TA) within 200 ms without pretreatments or chemical reagents. The FJH had the advantages of low energy consumption and being environmentally friendly. Compared with the rGO, the FCBG prepared by FJH was characterized by fewer defects, larger carbon sheets, and a turbostratic structure. Moreover, carbon steel Q235 was used as the substrate to prepare anti-corrosion coatings by mixing FCBG at different flash voltages with epoxy resin (EP). Based on this, the electrochemical performance of different coatings was compared before and after salt spray corrosion. The results demonstrated that the FCBG composite anti-corrosion coating (EP/$FCBG_{190}$) prepared using EP and FCBG synthesized at 190 V in the FJH, displayed stronger corrosion resistance than the EP and rGO composite coating (EP/rGO). The FJH synthesis process provides a feasible route for improving the synthesis process of the anti-corrosion coatings and the high value-added utilization of coal.

1. Introduction

Carbon steel has been widely used in construction and engineering structures due to its simple manufacturing process, relatively low cost, and good mechanical properties. However, the prolonged operation of carbon steel equipment would cause severe corrosion, resulting in equipment failure [1–4]. In recent years, there has been a growing focus on the development of anti-corrosion coatings to enhance the corrosion resistance of metal materials. Graphene is a carbon nanomaterial composed of carbon atoms in sp^2 hybridization mode, which has excellent thermal stability, impermeability, mechanical properties, and chemical stability. These characteristics make it a highly potential ultra-high anti-corrosion material [5–8]. A dense physical barrier layer forms by mixing graphene with epoxy resin (EP), so that the prepared anti-corrosion coating effectively blocks the penetration of small-molecule corrosive media, thereby enhancing its corrosion resistance [9–13]. Zheng et al. prepared composite anti-corrosion coatings on carbon steel substrates using urea-formaldehyde modified graphene oxide and EP [14]. Zhang et al. synthesized anti-corrosion coatings through in-situ polymerization of polyaniline/reduced graphene oxide (rGO)/$CePO_4$ and EP, and successfully applied them to Q235 carbon steel [15].

Traditional production processes include chemical vapor deposition [16,17], templated self-assembly [18,19], and chemical redox method [20,21]. However, the traditional production methods of graphene are time-consuming and energy intensive. Due to its costly and cumbersome production process, the traditional methods are not suitable for large-scale economical production of high-quality graphene. In summary, the traditional production processes are divided into two categories: bottom-up and top-down synthesis strategies. The bottom-up strategy is exemplified by chemical vapor deposition. To be specific, a thin film of graphene sheet is formed with individual carbon atoms at the bottom of the film. But once other impurity gases mix in the preparation process, the decline of graphene quality would be inevitable. Besides, this strategy also features the disadvantages of expensive equipment and high cost [22,23]. As for the top-down strategy, the mechanical exfoliation of graphite to form graphene sheets is taken as an example. The energy input required for forming graphene through the exfoliation of graphite would cause the sheets to crack and induce defects in the

* Corresponding author.
E-mail address: rtzhu2010@cumt.edu.cn (R. Zhu).

https://doi.org/10.1016/j.porgcoat.2023.107859
Received 14 May 2023; Received in revised form 31 July 2023; Accepted 1 August 2023
Available online 10 August 2023

graphene, which adversely affects its tensile strength. Meanwhile, the dispersion and stability of the graphene solution produced by this method are extremely low [24,25]. Therefore, it is essential to reduce CO_2 emissions and improve the performance of various applications of graphene by improving the synthesis process of graphene.

This study used Taixi anthracite (TA) as the carbon source to synthesize flash coal-based graphene (FCBG) with large carbon sheets and low defects by flash Joule heating (FJH) and applied it to anti-corrosion coatings successfully. It has been found that when the FJH releases current to the carbon source instantaneously, the carbon source would generate Joule heating in situ due to the internal resistance without any pretreatments, solvents, or catalysts. In addition, the heating and cooling rates (10^4 Ks^{-1}–10^5 Ks^{-1}) are extremely fast [26–28]. When the current passing through, TA generated Joule heating, making the carbon-based material reached a temperature above 2500 K within 200 ms. The extremely cooling rate (10^4 Ks^{-1}) made the turbostratic carbon layers composed of carbon atoms, thus forming wrinkled graphene. The unique turbine-layered structure of FCBG allowed it to maintain the optical and electronic properties of two-dimensional graphene even when hundreds of graphene layers were stacked [29,30]. And the output of the FJH depended on the carbon content of the raw material.

Because coal is a natural carbon source with large reserves and high carbon content, whose structure is more stable than that of biomass carbon sources. Accordingly, coal boasts great potential for conversion into graphene and possesses the advantage of low cost. Therefore, this study used TA as raw material, which is more suitable for obtaining high-yield FCBG. Compared with the traditional methods, the FJH had an extremely low demand for input energy, which was 1 kJ at most. As has been proved, the FJH is one of the most promising methods for large-scale economical synthesis of graphene. Being environmentally friendly and high yielding, it solely needs to input the raw materials. By comparing the electrochemical performances of the coating before and after salt spray corrosion, it was demonstrated that FCBG displayed better corrosion resistance than rGO, which greatly improved the corrosion resistance of the epoxy coating. Therefore, using FJH to synthesize FCBG from TA not only provides a feasible way for the high value-added utilization of coal but also offers a valuable reference for the green and sustainable development of graphene and the anti-corrosion coatings industry.

2. Experimental methods

2.1. Chemicals and materials

Epoxy resin (E51) and curing agent (T-31) were provided by Guangzhou Nashun Chemical Technology. Anhydrous ethanol, Sulfuric acid (H_2SO_4), and acetone (C_3H_6O) were purchased from Sinopharm Chemical Reagent. Deionized water was provided by Jiangsu Chemical Technology. All chemicals used in this study were analytically pure and did not require further purification.

2.2. Experimental methods

Firstly, 200 mg of TA was added into the quartz tube and then both ends of the quartz tube were closed with graphite block electrodes. To prevent sample leakage and quartz tube bursting, the samples were compressed by adjusting the spring, and the reaction chamber was evacuated to vacuum with a vacuum pump. Then the FJH system was charged to 190 V and pressed the discharge button to discharge the capacitor, the internal charge of the capacitor was discharged in less than 200 ms. During this process, the Joule heating generated by the sample itself caused the samples to rapidly heat up (10^5 Ks^{-1}) in less than 100 ms and cooled at an extremely fast rate (10^4 Ks^{-1}) to room temperature. Finally, $FCBG_{190}$ was obtained from the quartz tube. The samples made by 150 V were called $FCBG_{150}$.

2.3. Preparation of composite coating

10 mg of FCBG was ultrasonically treated in 10 ml of deionized water for 3 min, and 10 g of EP and 5 g of curing agent were added in turn. Then the mixture was sonicated for 5 min and stirred uniformly for 30 min. The mixture was left at room temperature for 30 min to remove bubbles generated by stirring. Finally, the mixture was applied on the surface of Q235 with a linear applicator and let stand for 24 h to obtain a dry film coating with a thickness of 50 ± 5 μm, marked as EP/FCBG. Different coatings were prepared by changing the coating materials, marked as EP/$FCBG_{150}$, EP/rGO, and EP/$FCBG_{190}$, respectively. The specific content of each coating was shown in Table S1.

2.4. Material characterization

SEM images were taken with a Zeiss Sigma 300 SEM system. A voltage of 10 keV was employed in the process of imaging. TEM and SAED images were obtained on a JEOL 2100 field emission transmission electron microscope at an acceleration voltage of 200 kV. XPS data were collected using a Thermo Scientific K-Alpha scanning X-ray microprobe with a base pressure of 5×10^{-9} Torr. Survey spectra and elemental spectra were recorded using 0.5 eV step sizes with a pass energy of 140 eV and 0.1 eV step sizes with a pass energy of 50 eV, respectively. All of the XPS spectra were corrected using the C 1s peaks (284.8 eV) as a reference. The FITR data were collected using Thermo Scientific Nicolet iS5, with spectra within the range of 4000–500 cm^{-1}. Powder XRD spectra were collected with a Bruker D8 advance diffractometer using zero background sample holders at a scan rate of 2°/min and a 0.1° step size. Raman spectra were collected by a Horiba Raman microscope outfitted with a 532 nm laser.

2.5. Electrochemical measurements

Electrochemical behaviors of all specimens in 0.5 M H_2SO_4 solution were measured by Corrtest CS450 electrochemical workstation through a three-electrode system. The coated carbon steels, Ag/AgCl electrode, and platinum plate (2 cm^2) acted as working electrodes, reference electrodes, and counter electrodes, respectively. The electrochemical impedance spectroscopy (EIS) data of specimens were measured at the frequency range of 10^{-2}–10^5 Hz under a sinusoidal perturbation of 15 mV amplitude of OCP. Additionally, the potentiodynamic polarization measurements were scanned under the set potential range of E_{ocp} ± 300 mV at the rate of 0.5 mV/s.

2.6. Simulation of flash Joule heating process

The structure of the flash graphene models was set as follows: the inner diameter and length of the quartz tube were set to 3 mm and 15 mm respectively, and the thickness was set to 1 mm. The radius and length of graphite electrodes were set to 3 mm and 5 mm. The radius and length of the intermediate samples were set to 3 mm and 5 mm, respectively. This finite element analysis was conducted based on the multi-physical field coupling of electromagnetic heat. One side of the electrode was set up for charging voltage and the other side was used for ground. The relevant properties of specific materials were shown in Table S2.

3. Results and discussion

3.1. Character of flash Joule heating process

In Fig. 1, the samples were directly placed in the quartz tube without pretreatment. The capacitor was first charged, and a path was formed with the samples when the discharge switch was pressed. Then the charge in the capacitor was released instantly. Due to the internal resistance of the samples, the passing current generated Joule heating in

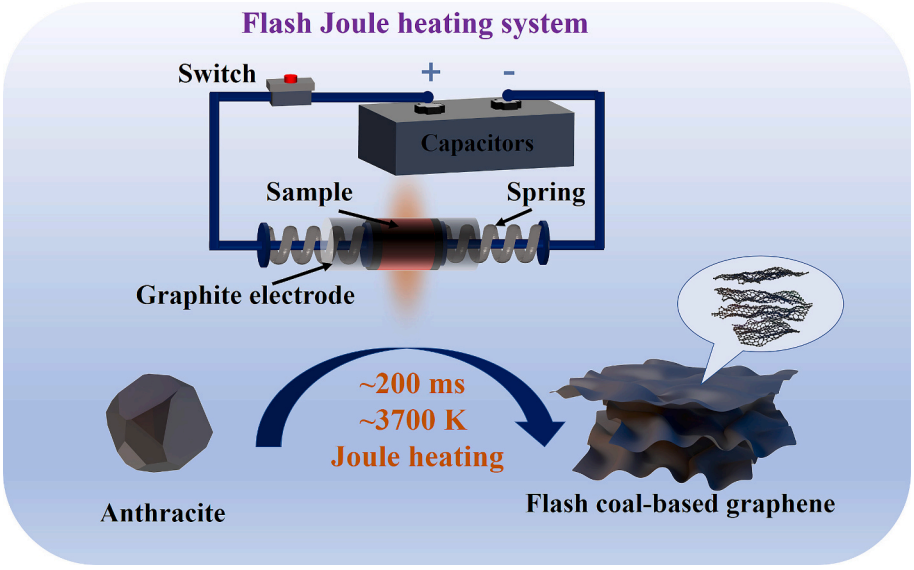

Fig. 1. Synthesis of FCBG by FJH system.

the samples, and the instantaneous temperature of the samples reached above 2500 K or even 3700 K within 200 ms. The high temperature and extremely high heating and cooling rates generated by Joule heating instantly transformed the TA particles into FCBG. The wrinkled and turbostratic nature of the graphene sheets endowed FCBG with the excellent performance of single-layer graphene.

As shown in Fig. 2(a–b), when the FJH flash voltage was 150 V, the instantaneous current passing through the samples reached 225 A, and the sample temperature rose to 2500 K within 200 ms and dropped to room temperature within 1 s. According to Eq. (1), it was calculated that the energy required for FJH to synthesize $FCBG_{150}$ was only 615 J. In Fig. 2(c–d), when the FJH synthesis voltage was increased to 190 V, the current passing through the samples reached 300 A. With this instantaneous high current, the sample temperature instantly rose to 3700 K within 200 ms, and the energy required for synthesizing $FCBG_{190}$ was calculated to be 1.02 kJ. As is proved, the FJH possesses the capability to control the sample temperature generated by the Joule heating by changing the flash voltage, and the energy needed for synthesis is very low.

To better explore the effect of the FJH flash voltage on the sample synthesis temperature, COMSOL software was used to conduct a finite element analysis on the FJH synthesis process. As shown in Fig. 2(e–f), the higher the FJH synthesis voltage was, the higher the sample heating rate was. Additionally, it quickly dropped to room temperature. The temperature at the center of the samples was the highest, the closer it was to the graphite electrode, the lower the sample temperature became. This proved that the Joule heating of the samples was first generated at the center, and then gradually spread to both ends. Meanwhile, by studying the distribution of the temperature field, it verified whether the Joule heating generated within the samples was uniformly distributed when the FJH was working. In Fig. 2(g–h), when the FJH was working, the temperature difference between the middle and both ends of the samples was not large in the longitudinal distribution, and the tangential distribution was consistent, which showed that the FJH realized the full reaction of all the samples in the quartz tube and thus ensured the high-quality FCBG. To verify the results of the simulation, the high-speed camera was used to record the FJH synthesis process. As shown in Fig. S1, a flash of light was generated at the center of the samples first, and then a dazzling light spot was produced on the entire samples at about 200 ms. Finally, the intensity of the light spot gradually weakens as the temperature of the samples decreased within 1 s. The observed results were consistent with the simulated results.

$$E = \left(V_1^2 - V_2^2\right) \times C/2 \quad (1)$$

where E denotes the energy of the capacitor discharge; V_1 represents the initial voltage; V_2 is the final voltage; and C denotes the capacitance capacity.

3.2. Influence of flash Joule heating on FCBG micromorphology

Microstructural changes in samples were observed by SEM. As shown in Fig. 3(a), due to the lower synthesis temperature, TA was mostly an amorphous carbon structure with low particle crystallinity. In Fig. 3 (b–d), after the FJH treatment, the carbon layer of FCBG displayed a wrinkled and turbostratic structure, and the surface crystallinity of the carbon layer was excellent with few defects. This is because when TA particles were treated by FJH, the instantaneous high temperature caused pyrolysis of the amorphous carbon structure to form the carbon six-membered ring structure, and the resulting graphitization repaired the existing defects. However, due to the extremely high cooling rate, there was insufficient time for the carbon six-membered ring structure to form the graphite structure with AB layers stacked, resulting in the disordered stacking of the sheets. This stacking method reduced the van der Waals force between the sheets, expended the interlayer spacing, and ultimately condensed to form this wrinkled graphene.

The surface morphology of TA and FCBG were better observed by TEM in Fig. 3(e–g). Due to the amorphous carbon structure of TA, too many stacked carbon layers lead to thicker sheets. However, the graphene sheets and lattice fringe structure were observed in FCBG, indicating that the graphene sheet of FCBG had good crystallinity, and there were almost no defects on the sheet surface. In Fig. S2, FCBG exhibited a more obvious lamellar structure and fewer surface defects than rGO. The SAED was used to confirm the existence of multiple overlapping crystal lattices in FCBG. The (001), (100), and (110) crystal plane structures were observed in Fig. 3(h) [31]. This explained the different lattice structures in FCBG and confirmed the turbostratic stacking mode of graphene sheets. The AFM image of FCBG was shown in Fig. 3(i). FCBG possessed a large sheet size and thin sheet thickness, which proved that the low number of stacked layers in FCBG makes it possible to maintain the excellent characteristics of graphene.

3.3. Influence of flash Joule heating on the chemical composition of FCBG

XPS was used to study the element proportion and atomic

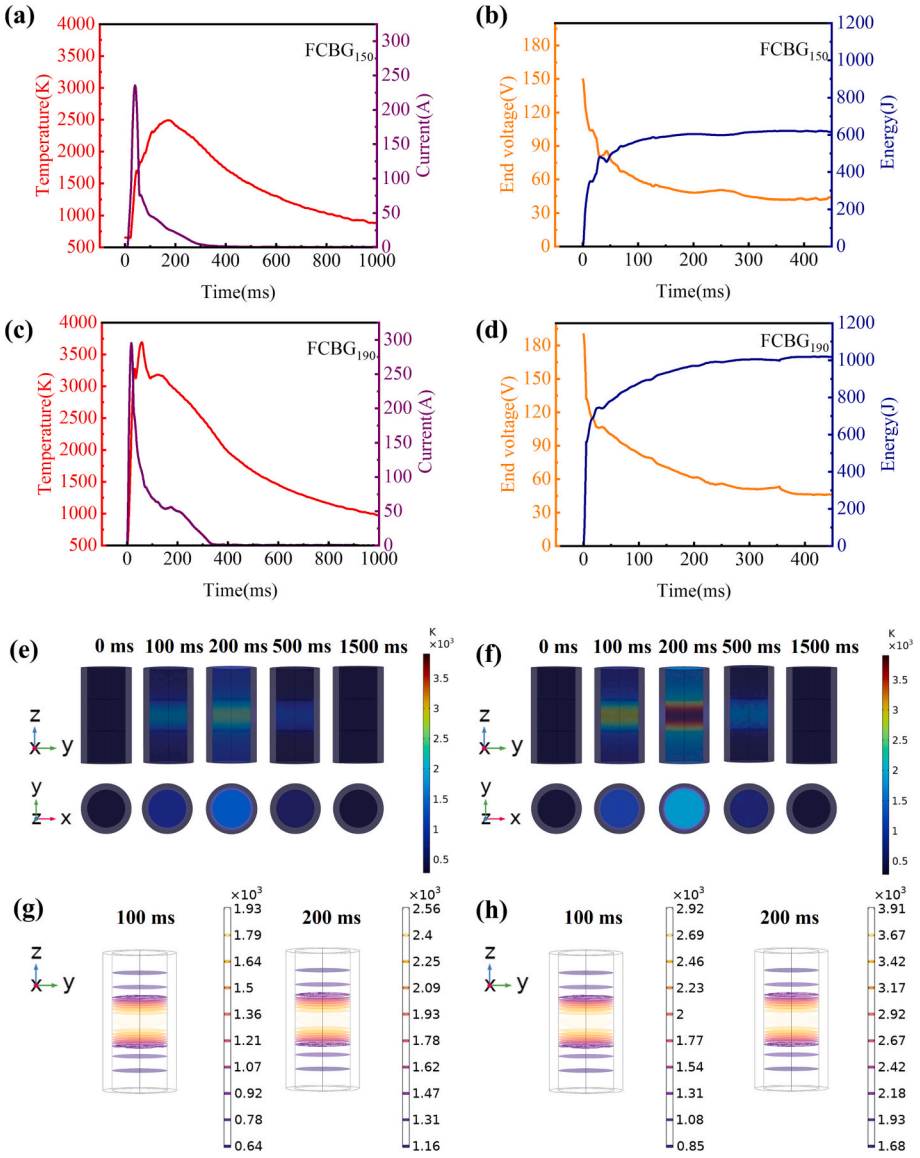

Fig. 2. (a–b) Electrical signal and energy when synthesizing $FCBG_{150}$, (c–d) Electrical signal, and energy when synthesizing $FCBG_{190}$, (e–f) Simulating the temperature change of synthetic $FCBG_{150}$ and $FCBG_{190}$, (g–h) Simulation of temperature field distribution of synthetic $FCBG_{150}$ and $FCBG_{190}$ (In order to better display the temperature field distribution of the sample, the quartz tube model is not shown).

hybridization of TA, $FCBG_{150}$, and $FCBG_{190}$. In Fig. S3, initially, TA contained impurities. The FJH treatment not only removed the impurities from FCBG but also endowed it with extremely high carbon content. This showed that in the FJH process, elements other than carbon were pyrolyzed and escaped at high temperatures, thus improving the purity of the samples. As shown in Fig. 4(a–c), by fitting the C1s spectrum of the samples, two peaks were observed, corresponding to sp^2 and sp^3 peaks, respectively; and the ratio of sp^2/sp^3 was positively correlated with the order of the samples [32,33]. Compared to TA, the sp^2 hybridization peaks of $FCBG_{150}$ and $FCBG_{190}$ after FJH treatment significantly increased, and while the sp^3 hybridization peaks decreased. With the increase of flash voltage, the sp^2 hybridization degree in the samples became higher. This is because the flash voltage was also positively correlated with the temperature. The Joule heating can make the carbon atoms enter the excited state, changing the bonding mode between the atoms so that FCBG shifts from sp^3 orbital hybridization to sp^2 orbital hybridization, which improves the order of FCBG.

Fig. 4(d) showed the FTIR spectra of rGO, TA, $FCBG_{150}$, and $FCBG_{190}$. For rGO, a series of distinct peaks were observed at 3418 cm^{-1}, 2914 cm^{-1}, 1384 cm^{-1}, and 1009 cm^{-1}, corresponding to -OH, $-CH_3$, C═O, and C—O [34–36]. It proved that TA and rGO possessed more sp^3 hybridized carbon atoms. Additionally, TA contained oxygen-containing functional groups. After FJH treatment, it was observed that the characteristic peak intensity of oxygen-containing functional groups of FCBG gradually weakened with the increase of voltage. This is because the oxygen-containing functional group bond on the surface of TA was broken at high temperatures, resulting in the formation of small molecules of water and carbon dioxide, which escaped from the TA's interior. This improved the order of the aromatic layer in FCBG accordingly, and it was observed that FCBG had a small characteristic peak due to the skeletal vibrations of unoxidized graphitic domains at 1640 cm^{-1}.

The degree of graphitization and the number of carbon layers of the samples were analyzed by XRD. As seen from Fig. 4(e), the XRD spectrum analysis of rGO showed that the diffraction peak of the (002) plane was far away from the typical diffraction peak (26°) of crystalline carbon, which confirmed that rGO hardly undergoes graphitization. However, the diffraction peak of the (002) plane was observed in FCBG after FJH treatment, which showed that FCBG had a better graphitization

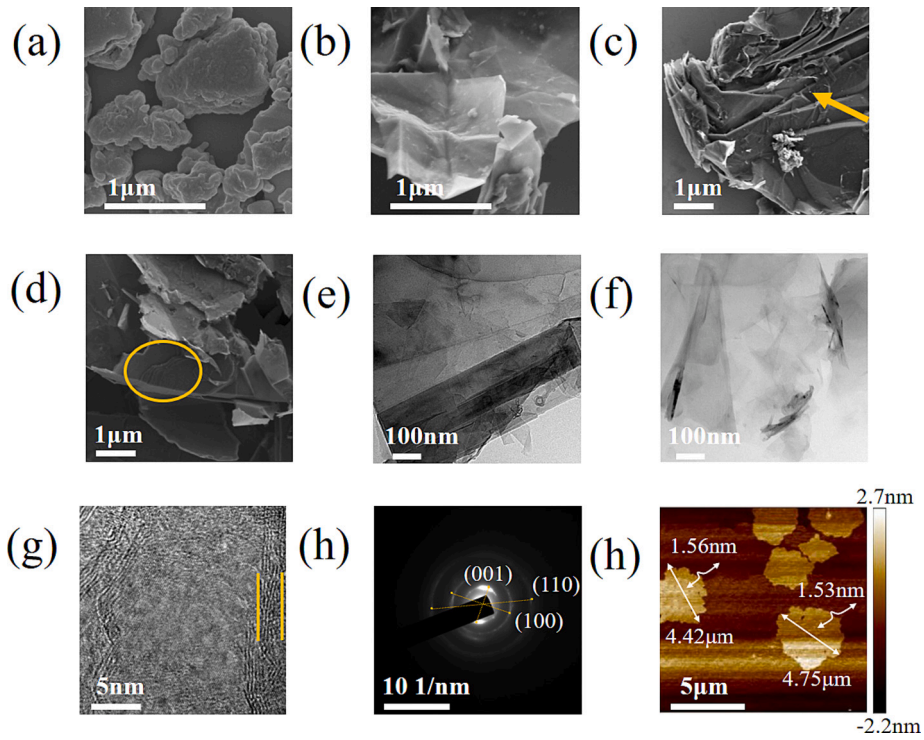

Fig. 3. Microstructural changes of TA after FJH treatment, (a) SEM image of TA, (b–d) SEM image of FCBG (The wrinkled graphene structure was shown by the arrows, and the disordered stacking of the sheets was shown by the circles) (e)TEM image of TA, (f–h) TEM image of FCBG. (Between the vertical lines is the Lattice fringe structure), (i) AFM image of FCBG.

degree and fewer defects than rGO. In addition, the fewer layers the samples had, the lower the diffraction peak intensity of the (002) plane and the wider FWHM became [37]. With the increase of the flash voltage, the diffraction peak intensity of the (002) plane of FCBG gradually decreased, and the FWHM width gradually increased, indicating that by increasing the flash voltage, not only can the surface defects of FCBG be reduced, but the turbostratic nature of FCBG can also be easily formed, making it easier for the carbon layer to peel off to form the graphene sheet, thereby reducing the thickness of the graphene layer of FCBG.

The quality of the graphene sheet and the degree of surface defects of the samples were judged by Raman. Fig. 4(f) showed the Raman spectra of different samples. In the standard Raman spectrum of graphene, three distinct characteristic peaks were found at 1341 cm^{-1}, 1580 cm^{-1}, and 2698 cm^{-1}, corresponding to the D peak, G peak, and 2D peak, respectively [38–40]. Generally, higher I_D/I_G represented more surface defects or more sp^3 hybrid clusters [41,42]. Because there were many defects in rGO and TA, it led to higher I_D/I_G. After the FJH treatment, the high temperature generated instantaneously by Joule heating caused the free radicals in TA to polymerize with carbon atoms, transforming some disordered structures such as amorphous and polyene vacancies into FCBG structures. Simultaneously, the size of sp^3 clusters gradually decreased, while the size of sp^2 clusters gradually increased. This phenomenon resulted in a reduction in the defect density on the sample surface. In Fig. 4(g), with the increase of flash voltage, the ratio of I_D/I_G of FCBG gradually decreased, which proved that FJH effectively reduced the surface defects of samples and improved the quality of samples by increasing flash voltage. The 2D peak is an important indicator to measure the number of graphene-stacked layers. The intensity of the 2D peak is negatively correlated with the number of graphene sheets in the samples, and positively correlated with the graphene performance of the samples. The intensity of the 2D peak in rGO was low due to the lower graphene quality and smaller sheet size, while the large amount of amorphous carbon structure in TA almost eliminated the 2D peak. Due to the turbostratic layout of the carbon layers of FCBG during the FJH treatment, the carbon layers were easier to be peeled off, which reduced the number of graphene-stacked layers of FCBG, and this layout enabled FCBG to exhibit good two-dimensional graphene electronic information. Therefore, FCBG witnessed a very high 2D peak.

By analyzing the correlation between the I_D/I_G of Raman spectroscopy and the graphite microcrystal size L (nm) obtained by XRD, the microcrystal base size of the carbon material was obtained [30].

$$L = 4.4(I_G/I_D) \quad (2)$$

According to Eq. (2), the crystallite size of the sample was inversely proportional to I_D/I_G. In Fig. 4(h), with the work of FJH, the L of the samples gradually increased from 1.77 nm at TA to 73.33 nm at $FCBG_{190}$. It showed that under the action of the Joule heating generated by FJH, the amorphous carbon in the sample would interact with each other so that the crystallite size of the samples gradually increased and transforms into a large-sheet graphene structure. The results proved that $FCBG_{190}$ synthesized by FJH had low-defect, high-quality, large-sheet graphene structures.

The TGA test was used to judge the organic composition of the samples. In Fig. 4(i), during the process of rising from room temperature to 600 °C, the small amount of volatile matter in TA was pyrolyzed at high temperature to produce gas, resulting in a gradual decrease in its mass. When the temperature was higher than 600 °C, the fixed carbon structure in TA was pyrolyzed, and the mass decreased rapidly. When FJH synthesized $FCBG_{190}$, the instantaneous high temperature caused all the volatile matter to be pyrolyzed, and the amorphous carbon structure had been transformed into the graphene structure, and the structure of $FCBG_{190}$ was relatively stable. The test showed that before 700 °C, the quality of $FCBG_{190}$ hardly decreased, and the temperature of carbon pyrolysis was much higher than that of TA, proving that the structural stability of $FCBG_{190}$ was significantly greater than that of TA, and there was almost no volatile matter, which ensured the purity of graphene.

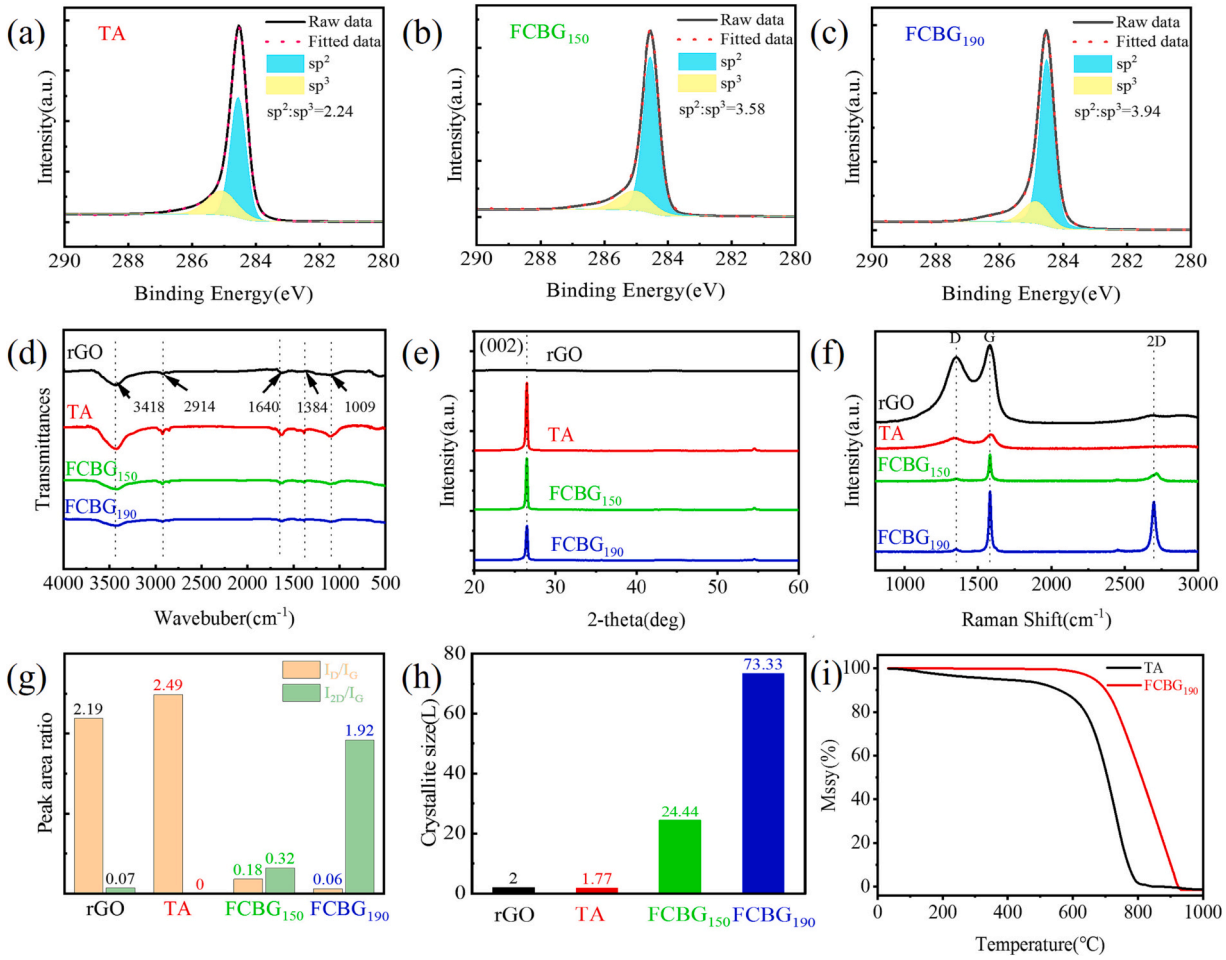

Fig. 4. (a–c) The change of sp^2 hybridization peak and sp^3 hybridization peak of TA, $FCBG_{150}$, $FCBG_{190}$, (d) FITR spectra of TA, $FCBG_{150}$, $FCBG_{190}$, rGO, (e) XRD spectra of TA, $FCBG_{150}$, $FCBG_{190}$, rGO, (f) Raman spectra of TA, $FCBG_{150}$, $FCBG_{190}$, rGO, (g) I_D/I_G, I_{2D}/I_G of TA, $FCBG_{150}$, $FCBG_{190}$, rGO after Raman data fitting, (h) Crystallite size of TA, $FCBG_{150}$, $FCBG_{190}$, rGO, (i) TGA curves of TA and $FCBG_{190}$.

3.4. Anti-corrosion properties of different coatings

The distribution of different samples in EP was investigated by observing the SEM of the coating cross-section. It could be seen from Fig. 5 that the cross-section of the pure EP coating had a lot of porous structure during the curing of the coating. The incorporation of rGO was well mixed with EP, and the pores of the contact boundary were small. However, the contact between TA or $FCBG_{150}$ and EP was inadequate, whose interface produced a large pore structure. The results indicated that the distribution of TA and $FCBG_{150}$ in EP was not uniform, which reduced the barrier effect of the coating. Compared with other samples, $FCBG_{190}$ had the closest contact with EP, and there were almost no pores in the contact. It proved that the distribution of $FCBG_{190}$ in EP was the most uniform, and it effectively prevented the infiltration of corrosive media.

Fig. 6 showed the adhesion of anti-corrosion coatings with different materials added to epoxy resin. Due to the poor distribution of TA and $FCBG_{150}$ in epoxy, many pores were produced in the coating, which made the adhesion of the coating to carbon steel substrate very low. Compared with rGO, $FCBG_{190}$ had a larger lamellar size, and $FCBG_{190}$ was well distributed in EP and closely adhered to EP. Therefore, the EP/$FCBG_{190}$ coating exhibited the strongest adhesion and had the best corrosion resistance in the long-term corrosion environment.

A salt fog test was conducted to simulate the corrosion resistance of the coated samples in a heavy corrosion environment characterized by heavy salt, high temperature, and high humidity. The saturated NaCl solution was used in the corrosive environment with the experimental temperature at 40 °C and the duration of continuous corrosion for 7

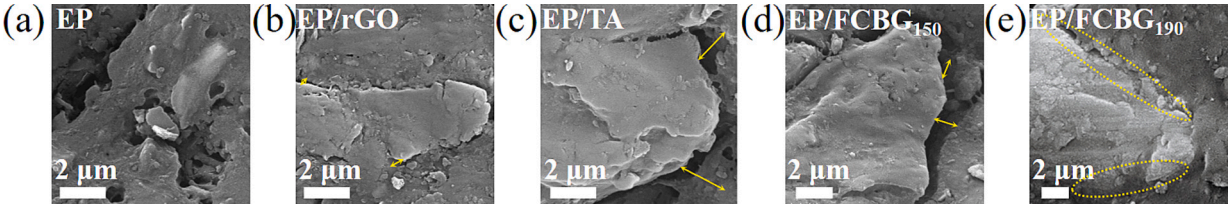

Fig. 5. (a–e) SEM images of distribution of rGO, TA, $FCBG_{150}$, $FCBG_{190}$ in epoxy resin (the yellow arrows indicate the pores between the samples and EP, and yellow circles indicate areas where $FCBG_{190}$ has excellent contact with EP). (For interpretation of the references to colour in this figure legend, the reader is referred to the web version of this article.)

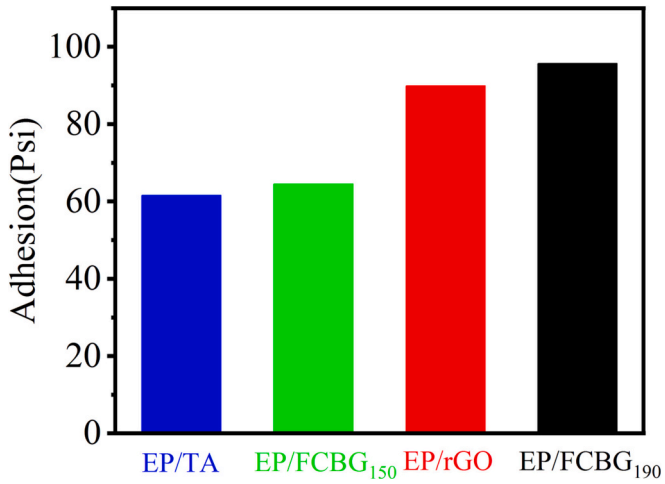

Fig. 6. Adhesion of coatings with different materials added to epoxy.

days.

Fig. 7 showed the OCP data of different coatings before and after the salt spray test, which was used to evaluate the corrosion trend. The comparison revealed that the OCP of the Q235 is −0.459 V before the salt spray test and −0.513 V after the salt spray test. Additionally, the OCP of FCBG coating after FJH treatment before and after the salt spray was much larger than that of TA coating. $FCBG_{190}$ coating consistently maintained the highest OCP, which proved that reducing the surface defects of TA by the FJH greatly weakened the corrosion tendency of the samples, and $FCBG_{190}$ had stronger corrosion resistance than rGO [43].

EIS was employed to evaluate the long-term anti-corrosion performance of different coatings. The size of the capacitive arcs reflected the speed of corrosion product diffusion and the ease of charge transfer. Accordingly, the size of the capacitance arc radius was used to judge the strength of the anti-corrosion layer. In Fig. S4, the arc radius of EP/$FCBG_{190}$ and EP/rGO coatings remained similar both before and after salt spray corrosion. Compared with that of other coatings, they maintained the largest. It proved that EP/$FCBG_{190}$ and EP/rGO effectively protected the Q235 substrate in a corrosive environment.

The barrier performance of coatings was semi-quantitatively represented by the impedance moduli at 0.01 Hz ($|Z|_{0.01\ Hz}$). In Fig. 8(a–b), the matrix Q235 exhibited the lowest $|Z|_{0.01\ Hz}$ value ($5.8 \times 10^2\ \Omega{\cdot}cm^2$) among all the samples due to the strong corrosive effect of the acidic environment on metallic materials. The anti-corrosion performance was improved after adding the coating. For the Pure EP, EP/TA, and EP/

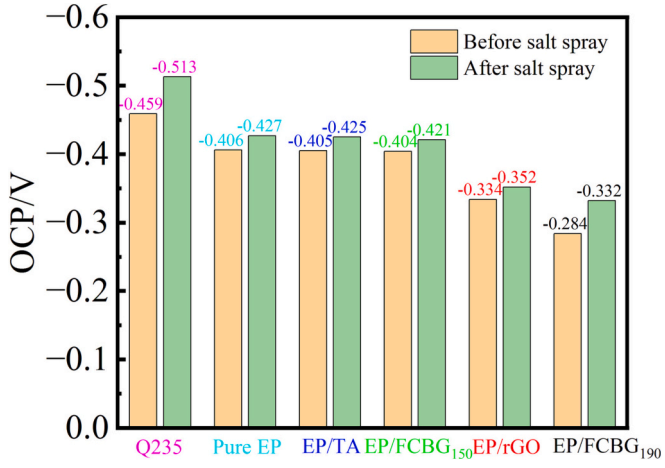

Fig. 7. Comparison of OCP of different anti-corrosion coatings before and after salt spray.

$FCBG_{150}$ coatings, the impedance moduli at the lowest frequency exhibited fast reductions with the immersion time, and the capacitive loops also gradually diminished. These observations indicated the inferior protective abilities of the Pure EP, EP/$FCBG_{150}$ coatings for steel plates. This might be due to the pore structures formed on the surface of Pure EP during curing and the uneven distribution of $FCBG_{150}$ in EP compared to rGO and $FCBG_{190}$, which cannot effectively form a dense graphene network to prevent the entry of corrosive media. In the long-term corrosion process, the low adhesion of Pure EP and EP/$FCBG_{150}$ coatings to carbon steel would cause the coating to fall off, and the corrosive medium would directly corrode the carbon steel substrate. However, the EP/rGO and EP/$FCBG_{190}$ not only exhibited relatively straighter Bode impedance lines over a wide frequency range after 7 days of immersion but also had a bigger $|Z|_{0.01\ Hz}$ value. These results revealed that the large graphene sheet size and low defect density in $FCBG_{190}$ prevented the infiltration of small molecular corrosive substances, resulting in the excellent and stable protection ability of $FCBG_{190}$ compared with rGO in terms of long-term corrosion. As shown in Fig. 8(c–d), the higher phase angled after the salt spray test also indicated that EP/$FCBG_{190}$ had long-term anti-corrosion performance.

For a further study of the anti-corrosion performance of different coated samples, the EIS data were fitted via Zview software using two types of electrical equivalent circuits. The circuit in Fig. 9(a) represented the initial stage of the Q235 substrate being uncorroded, and the circuit in Fig. 9(b) represented the stage when the corrosion had progressed to the coating and the steel plate. In the circuit, Rs, R_p (R_c), R_{ct}, $CPE_{coat,}$ and CPE_{dl} represented the solution resistance, coating pore resistance, charge transfer resistance, coating constant phase, and double-layer constant phase, respectively. The constant phase element (n) was used to correct the deviation of the ideal capacitance. The equivalent circuit fitting data of different coatings at the initial stage of salt spray corrosion were shown in Table S3. The R_c of EP/$FCBG_{190}$ and EP/rGO were comparable and three orders of magnitude higher than that of Pure EP coating, which proved that the introduction of $FCBG_{190}$ improved the corrosion resistance of the coating.

Usually, R_p and R_{ct} are regarded as indicators to evaluate coated samples' barrier properties. The higher R_p and R_{ct} imply that it is more difficult for the corrosive media to penetrate the coating. As shown in Table 1, as the salt spray corrosion progressed, the R_p and R_{ct} of the coating gradually decreased. After 7 days of corrosion, EP/$FCBG_{190}$ synthesized by FJH shows higher R_p and R_{ct} than EP/rGO, proving that EP/$FCBG_{190}$ had a stronger barrier effect on corrosive media [44]. This is because EP/$FCBG_{190}$ had a larger sheet size and fewer defects, and the turbostratic stacking of graphene sheets hindered the penetration of corrosive media and the transfer between charges. Although the anti-corrosion effect of $FCBG_{150}$ was inadequate, it still achieved the anti-corrosion effect of rGO by increasing the flash voltage. In addition, the CPE_{dl} of EP/$FCBG_{190}$ was comparable to that of rGO, and the CPE_{dl} of TA decreased by three orders of magnitude after FJH treatment. This indicated that EP/$FCBG_{190}$ had stronger adhesion to metal substrates and better anti-corrosion performance on the substrate in a long-term corrosion environment.

The actual situation of different coatings after salt spray corrosion was shown in Fig. 10(a). After 7 days of corrosion, as the corrosion medium had completely penetrated the metal matrix, the coating of Pure EP, EP/TA, EP/$FCBG_{150}$ had been completely peeled off. Due to the more defects and smaller sheet size on the EP/rGO surface, the corrosive medium also caused part of the coating to peel off. However, EP/$FCBG_{190}$ showed strong corrosion resistance: not only does the coating not fall off, but also the corroded area of the metal substrate was very small, which is consistent with the results of the EIS analysis.

Fig. 10(b) showed the polarization curve of the coated samples. We found that EP/$FCBG_{190}$ and EP/rGO had lower corrosion potential, which proved that the coated samples had the best corrosion resistance. Fig. 10(c–d) showed the corrosion parameters obtained by fitting. After FJH treatment, the corrosion current density of TA was reduced by three

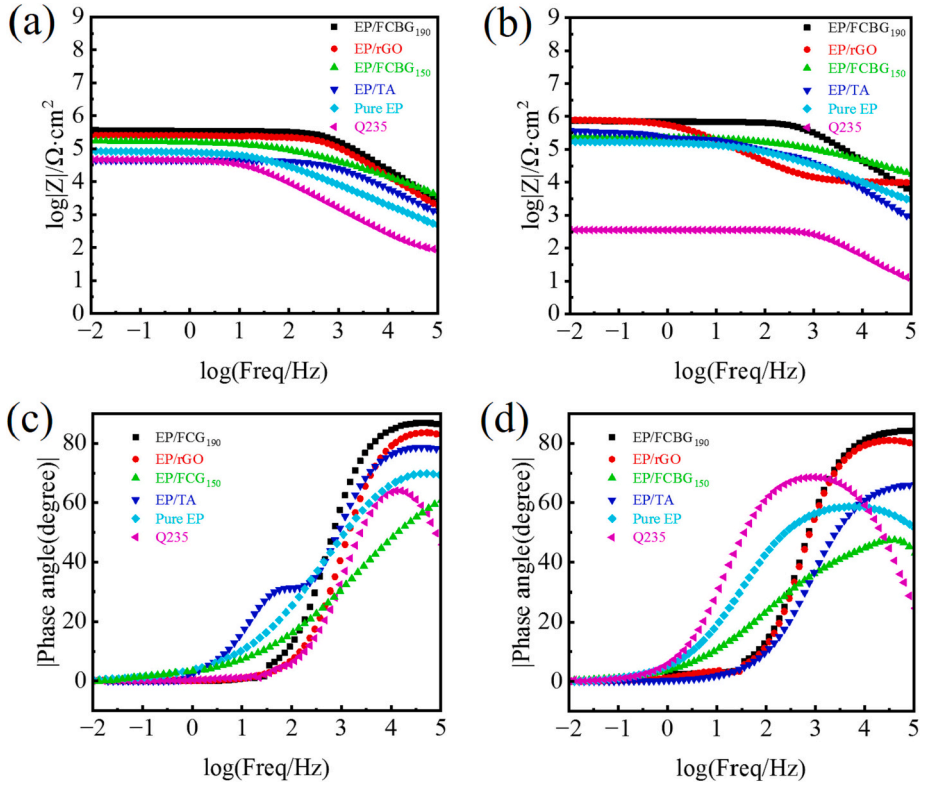

Fig. 8. (a–b) log|Z|-Frequency of samples before and after salt spray corrosion, (c–d) Phase-diagram of samples before and after salt spray corrosion (The electrochemical tests were carried out in 0.5 M H_2SO_4 electrolyte solution).

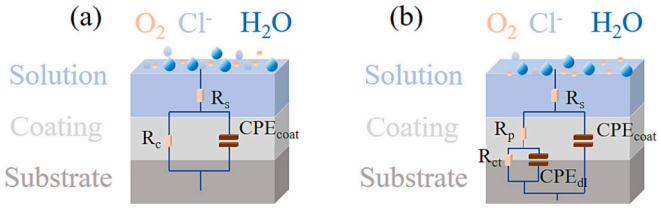

Fig. 9. The proposed electrical equivalent circuits for EIS results. (a) Q235 has no corrosion stage, (b) Corrosion phase occurs between coating and Q235.

orders of magnitude, which greatly reduced the corrosion rate of the coating. Compared with EP/rGO, EP/$FCBG_{190}$ still exhibited a larger corrosion voltage (−0.328 V) and lower corrosion current density (4.457×10^{-8} A/cm^2). This is because $FCBG_{190}$ had a higher anti-corrosion resistance in EP coating, which greatly slowed down the charge transfer rate of corrosive media when they passed through EP/$FCBG_{190}$ coating.

3.5. Protective mechanisms of EP/$FCBG_{190}$ coating

Fig. 11 showed the corrosion protection mechanism of Pure EP coating on metal substrates before and after adding FCBG. In Fig. 11(a), EP formed many small defects during the curing process, which affected the compactness of the coating and allowed corrosive media (such as Cl^-, H_2O, and O_2) to enter the metal surface through these defects to cause corrosion. However, the addition of $FCBG_{190}$ effectively reduced the tiny defects in the coating curing process and improved the corrosion resistance of the coating. In Fig. 11(b), compared with rGO, $FCBG_{190}$ had fewer surface defects and a larger graphene sheet size. Moreover, the turbostratic stacking of graphene sheets enabled $FCBG_{190}$ to form a dense graphene network in EP, making it difficult for the corrosion medium to contact the metal substrate and thus improving the anti-corrosion performance.

4. Conclusion

In this study, with TA as raw material, the low-defect, large-sheet FCBG was successfully synthesized by FJH within 200 ms without adding any chemical reagents and pretreatment. The energy required for the synthesis of $FCBG_{190}$ was only 1.02 kJ. The finite element analysis of

Table 1
Electrochemical parameters fitted by electrochemical EIS tests of different coatings after salt spray corrosion.

	CPE_{coat}		CPE_{dl}		R_p (Ω.cm^{-2})	R_{ct} (Ω.cm^{-2})
	$Y_0(\Omega^{-1}cm^{-2}s^n)$	n_{coat}	$Y_0(\Omega^{-1}cm^{-2}s^n)$	n_{dl}		
Q235	4.67×10^{-4}	0.958	3.65×10^{-3}	0.984	15,975	705
Pure EP	3.70×10^{-6}	0.998	6.05×10^{-5}	0.795	78,743	1470
EP/TA	8.43×10^{-6}	0.998	7.86×10^{-6}	0.690	91,130	2815
EP/$FCBG_{150}$	1.43×10^{-6}	0.942	2.22×10^{-7}	0.989	138,350	4001
EP/rGO	2.33×10^{-9}	0.989	2.24×10^{-9}	0.875	227,780	23,422
EP/$FCBG_{190}$	1.63×10^{-9}	0.946	2.08×10^{-9}	0.905	335,010	35,250

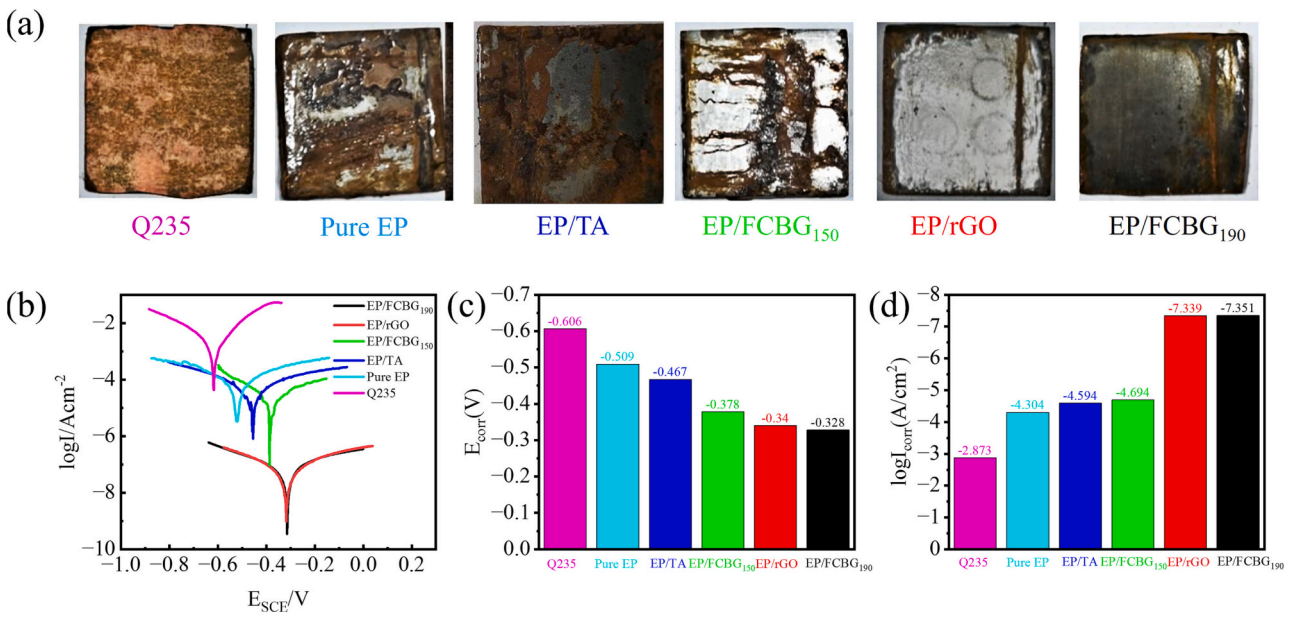

Fig. 10. (a) Surface changes of different coatings after salt spray corrosion for 7 days, (b) Polarization curves and fitted self-corrosion voltage and current of different coatings after salt spray test.

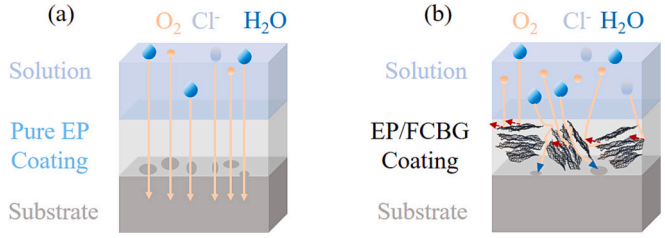

Fig. 11. Schematic diagram of salt spray corrosion. (a) Pure EP coating, (b) EP/$FCBG_{190}$ coating.

the FJH process was carried out, and the results verified that the temperature field distribution in the FJH synthesis process was uniform. Finally, the FCBGs prepared with different flash voltages were applied to anti-corrosion coatings, and the electrochemical performance of different coatings after 7 days of salt spray corrosion was analyzed. The results showed that the corrosion resistance of the FCBG coating had been greatly improved. The extremely low defects and large-sized graphene sheets of $FCBG_{190}$ effectively prevented the infiltration of corrosive media. Compared with rGO, $FCBG_{190}$ displayed better performance in corrosion resistance. The ease of synthesis, high-quality graphene, and low energy consumption indicate that the FJH system is a green and efficient way for large-scale production of flash graphene, greatly reducing energy waste and ensuring an excellent application prospect.

CRediT authorship contribution statement

Yuntian Liao: Conceptualization, Methodology, Validation, Investigation, Writing – original draft, Funding acquisition, Project administration. **Rongtao Zhu:** Investigation, Validation, Writing – review & editing, Funding acquisition, Project administration. **Wenjun Zhang:** Supervision, Writing – review & editing. **Zhuang Liu:** Software, Validation. **Haiyang Zhu:** Software. **Yang Sun:** Investigation.

Declaration of competing interest

The authors declare that they have no known competing financial interests or personal relationships that could have appeared to influence the work reported in this paper.

Data availability

Data will be made available on request.

Acknowledgments

This work was supported by National Natural Science Foundation of China (51974307), Key Research and Development Project of Xuzhou City (KC21287).

Appendix A. Supplementary data

Supplementary data to this article can be found online at https://doi.org/10.1016/j.porgcoat.2023.107859.

References

[1] C. Xing, Z. Zhang, L. Yu, G.I.N. Waterhouse, L. Zhang, Anti-corrosion performance of nanostructured poly (aniline-co-metanilic acid) on carbon steel, Prog. Org. Coat. 77 (2014) 354–360, https://doi.org/10.1016/j.porgcoat.2013.10.010.
[2] L. Li, Y. Shi, Z. Xu, H. Sun, M.D.S. Amin, X. Yang, F. Guo, W. Shi, Environmentally friendly synthesis of oxygen-doped g-C_3N_4 nanosheets for enhancing photocatalytic corrosion resistance of carbon steel, Prog. Org. Coat. 163 (2022), 106628, https://doi.org/10.1016/j.porgcoat.2021.106628.
[3] D. Dwivedi, K. Lepková, T. Becker, Carbon steel corrosion: a review of key surface properties and characterization methods, RSC Adv. 7 (2017) 4580–4610, https://doi.org/10.1039/c6ra25094g.
[4] N.R. Baddoo, Stainless steel in construction: a review of research, applications, challenges and opportunities, J. Constr. Steel Res. 64 (2008) 1199–1206, https://doi.org/10.1016/j.jcsr.2008.07.011.
[5] S. Liu, T.J. Pan, R.F. Wang, Y. Yue, J. Shen, Anti-corrosion and conductivity of the electrodeposited graphene/polypyrrole composite coating for metallic bipolar plates, Prog. Org. Coat. 136 (2019), 105237, https://doi.org/10.1016/j.porgcoat.2019.105237.
[6] V. Veloso, F. Cotting, D. Silva, A. Santos, Graphene and PANI functionalization with myristic acid for incorporation in anti-corrosion epoxy coatings, Prog. Org. Coat. 172 (2022), 107146, https://doi.org/10.1016/j.porgcoat.2022.107146.
[7] R. Ding, S. Chen, J. Lv, W. Zhang, X. Zhao, J. Liu, X. Wang, T. Gui, B. Li, Y. Tang, W. Li, Study on graphene modified organic anti-corrosion coatings: a comprehensive review, J. Alloy. Compd. 806 (2019) 611–635, https://doi.org/10.1016/j.jallcom.2019.07.256.
[8] J. Mu, F. Gao, G. Cui, S. Wang, S. Tang, Z. Li, A comprehensive review of anticorrosive graphene-composite coatings, Prog. Org. Coat. 157 (2021), 106321, https://doi.org/10.1016/j.porgcoat.2021.106321.

[9] G. Cui, Z. Bi, R. Zhang, J. Liu, X. Yu, Z. Li, A comprehensive review on graphene-based anti-corrosive coatings, Chem. Eng. J. 373 (2019) 104–121, https://doi.org/10.1016/j.cej.2019.05.034.
[10] C. Zhang, W. Li, C. Liu, C. Zhang, L. Cao, D. Kong, W. Wang, S. Chen, Effect of covalent organic framework modified graphene oxide on anticorrosion and self-healing properties of epoxy resin coatings, J. Colloid. Interf. Sci. 608 (2022) 1025–1039, https://doi.org/10.1016/j.jcis.2021.10.024.
[11] L. Zhou, P. Zhang, L. Shen, L. Chu, J. Wu, Y. Ding, B. Zhong, X. Zhang, N. Bao, Modified graphene oxide/waterborne epoxy composite coating with enhanced corrosion resistance, Prog. Org. Coat. 172 (2022), 107100, https://doi.org/10.1016/j.porgcoat.2022.107100.
[12] Y. Wu, J. Yu, W. Zhao, C. Wang, B. Wu, G. Lu, Investigating the anti-corrosion behaviors of the waterborne epoxy composite coatings with barrier and inhibition roles on mild steel, Prog. Org. Coat. 133 (2019) 8–18, https://doi.org/10.1016/j.porgcoat.2019.04.028.
[13] H. Wu, L. Cheng, C. Liu, X. Lan, H. Zhao, Engineering the interface in graphene oxide/epoxy composites using bio-based epoxy-graphene oxide nanomaterial to achieve superior anticorrosion performance, J. Colloid. Interf. Sci. 587 (2021) 755–766, https://doi.org/10.1016/j.jcis.2020.11.035.
[14] H. Zheng, Y. Shao, Y. Wang, G. Meng, B. Liu, Reinforcing the corrosion protection property of epoxy coating by using graphene oxide-poly(urea-formaldehyde) composites, Corros. Sci. 123 (2017) 267–277, https://doi.org/10.1016/j.corsci.2017.04.019.
[15] X. Zhang, B. Li, T. Chen, X. Ke, R. Xiao, Study on $CePO_4$ modified PANI/RGO composites to enhance the anti-corrosion property of epoxy resin, Prog. Org. Coat. 178 (2023), 107472, https://doi.org/10.1016/j.porgcoat.2023.107472.
[16] S. Ullah, M. Hasan, H.Q. Ta, L. Zhao, Q. Shi, L. Fu, J. Choi, R. Yang, Z. Liu, M. H. Rümmeli, Synthesis of doped porous 3D graphene structures by chemical vapor deposition and its applications, Adv. Funct. Mater. 29 (2019) 1904457, https://doi.org/10.1002/adfm.201904457.
[17] H. Wang, X. Mi, Y. Li, S. Zhan, 3D graphene-based macrostructures for water treatment, Adv. Mater. 32 (2020) 1806843, https://doi.org/10.1002/adma.201806843.
[18] J. Cai, Z. Zhang, S. Yang, Y. Min, G. Yang, K. Zhang, Self-conversion templated fabrication of sulfur encapsulated inside the N-doped hollow carbon sphere and 3D graphene frameworks for high-performance lithium-sulfur batteries, Electrochim. Acta 295 (2019) 900–909, https://doi.org/10.1016/j.electacta.2018.11.013.
[19] L. Liu, X. Li, G. Zhang, Z. Zhang, C. Fang, H. Ma, W. Luo, Z. Liu, Enhanced stability lithium-ion battery based on optimized graphene/Si nanocomposites by templated assembly, Acs. Omega. 4 (2019) 18195–18202, https://doi.org/10.1021/acsomega.9b02089.
[20] F.M. Vivaldi, A. Dallinger, A. Bonini, N. Poma, L. Sembranti, D. Biagini, P. Salvo, F. Greco, F. Di Francesco, Three-dimensional (3D) laser-induced graphene: structure, properties, and application to chemical sensing, Acs. Appl. Mater. Inter. 13 (2021) 30245–30260, https://doi.org/10.1021/acsami.1c05614.
[21] R. You, Y.Q. Liu, Y.L. Hao, D.D. Han, Y.L. Zhang, Z. You, Laser fabrication of graphene-based flexible electronics, Adv. Mater. 32 (2020) 1901981, https://doi.org/10.1002/adma.201901981.
[22] Y. Tao, Z. Sui, B. Han, Advanced porous graphene materials: from in-plane pore generation to energy storage applications, J. Mater. Chem. A 8 (2020) 6125–6143, https://doi.org/10.1039/d0ta00154f.
[23] T. Wang, J. Li, Y. Zhang, F. Liu, B. Zhang, Y. Wang, R. Jiang, G. Zhang, R. Sun, C. P. Wong, Highly ordered 3D porous graphene sponge for wearable piezoresistive pressure sensor applications, Chem-Eur. J. 25 (2019) 6378–6384, https://doi.org/10.1002/chem.201900014.
[24] S. Wang, X. Wang, C. Sun, Z. Wu, Room-temperature fast assembly of 3D macroscopically porous graphene frameworks for binder-free compact supercapacitors with high gravimetric and volumetric capacitances, J. Energy. Chem. 61 (2021) 23–28, https://doi.org/10.1016/j.jechem.2021.01.019.
[25] X. Wu, F. Mu, H. Zhao, Recent progress in the synthesis of graphene/CNT composites and the energy-related applications, J. Mater. Sci. Technol. 55 (2020) 16–34, https://doi.org/10.1016/j.jmst.2019.05.063.
[26] W.A. Algozeeb, P.E. Savas, Z. Yuan, Plastic waste product captures carbon dioxide in nanometer pores, ACS Nano 16 (2022) 7284–7290, https://doi.org/10.1021/acsnano.0c06328.
[27] K.M. Wyss, W. Chen, J.L. Beckham, Holey and wrinkled flash graphene from mixed plastic waste, ACS Nano 16 (2022) 7804–7815, https://doi.org/10.1021/acsnano.2c00379.
[28] W. Chen, J.T. Li, Z. Wang, Ultrafast and controllable phase evolution by flash joule heating, ACS Nano 15 (2021) 11158–11167, https://doi.org/10.1021/acsnano.1c03536.
[29] P. Huang, R. Zhu, X. Zhang, W. Zhang, A milliseconds flash joule heating method for the regeneration of spent cathode carbon, J. Environ. Sci. Heal. A. 57 (2022) 33–44, https://doi.org/10.1080/10934529.2021.2022422.
[30] P. Huang, R. Zhu, X. Zhang, W. Zhang, Effect of free radicals and electric field on preparation of coal pitch-derived graphene using flash Joule heating, Chem. Eng. J. 450 (2022), 137999, https://doi.org/10.1016/j.cej.2022.137999.
[31] J. Liu, Q. Ma, Z. Huang, G. Liu, H. Zhang, Recent progress in graphene-based noble-metal nanocomposites for electrocatalytic applications, Adv. Mater. 31 (2019) 1800696, https://doi.org/10.1002/adma.201800696.
[32] V. Vatanpour, S.S.M. Khadem, A. Dehqan, M.A. Al-Naqshabandi, M.R. Ganjali, S. S. Hassani, M.R. Rashid, M.R. Saeb, N. Dizge, Efficient removal of dyes and proteins by nitrogen-doped porous graphene blended polyethersulfone nanocomposite membranes, Chemosphere 263 (2021), 127892, https://doi.org/10.1016/j.chemosphere.2020.127892.
[33] B. Moeini, M.R. Linford, N. Fairley, A. Barlow, P. Cumpson, D. Morgan, V. Fernandez, J. Baltrusaitis, Definition of a new (Doniach-Sunjic-Shirley) peak shape for fitting asymmetric signals applied to reduced graphene oxide/graphene oxide XPS spectra, Surf. Interface Anal. 54 (2022) 67–77, https://doi.org/10.1002/sia.7021.
[34] A. Konwar, S. Kalita, J. Kotoky, D. Chowdhury, Chitosan-iron oxide coated graphene oxide nanocomposite hydrogel: a robust and soft antimicrobial biofilm, Acs. Appl. Mater. Inter. 8 (2016) 20625–20634, https://doi.org/10.1021/acsami.6b07510.
[35] H. Liu, T. Kuila, N.H. Kim, B. Ku, J.H. Lee, In situ synthesis of the reduced graphene oxide-polyethyleneimine composite and its gas barrier properties, J. Mater. Chem. A 1 (2013) 3739–3746, https://doi.org/10.1039/c3ta01228j.
[36] G. Goncalves, P.A. Marques, C.M. Granadeiro, H.I. Nogueira, M.K. Singh, J. Gracio, Surface modification of graphene nanosheets with gold nanoparticles: the role of oxygen moieties at graphene surface on gold nucleation and growth, Chem. Mater. 21 (2009) 4796–4802, https://doi.org/10.1021/cm901052s.
[37] S. Kapoor, A. Jha, H. Ahmad, S.S. Islam, Avenue to large-scale production of graphene quantum dots from high-purity graphene sheets using laboratory-grade graphite electrodes, Acs. Omega. 5 (2020) 18831–18841, https://doi.org/10.1021/acsomega.0c01993.
[38] N. Kumar, R. Pandian, P.K. Das, T.R. Ravindran, S. Dash, A.K. Tyagi, High-temperature phase transformation and low friction behaviour in highly disordered turbostratic graphite, J. Phys. D. Appl. Phys. 46 (2013), 395305, https://doi.org/10.1088/0022-3727/46/39/395305.
[39] W. Bao, Z. Wang, B. Hu, D. Tang, Thermal transport across graphene/GaN and MoS_2/GaN interfaces, Int. J. Heat. Mass. Tran. 201 (2023), 123569, https://doi.org/10.1016/j.ijheatmasstransfer. 2022.123569.
[40] A.C. Ferrari, J.C. Meyer, V. Scardaci, C. Casiraghi, M. Lazzeri, F. Mauri, S. Piscanec, D. Jiang, K.S. Novoselov, S. Roth, Raman spectrum of graphene and graphene layers, Phys. Rev. Lett. 97 (2006), 187401, https://doi.org/10.1103/PhysRevLett.97.187401.
[41] C. Muñoz-Ferreiro, C. López-Pernía, Á. Gallardo-López, R. Poyato, Unravelling the optimization of few-layer graphene crystallinity and electrical conductivity in ceramic composites by Raman spectroscopy, J. Eur. Ceram. Soc. 41 (2021) 290–298, https://doi.org/10.1016/j.jeurceramsoc.2021.09.025.
[42] D.L. Silva, J.L.E. Campos, T.F.D. Fernandes, J.N. Rocha, L.R.P. Machado, E. M. Soares, D.R. Miquita, H. Miranda, C. Rabelo, O.P. Vilela Neto, A. Jorio, L. G. Cançado, Raman spectroscopy analysis of number of layers in mass-produced graphene flakes, Carbon 161 (2020) 181–189, https://doi.org/10.1016/j.carbon.2020.01.050.
[43] M. Ramezanzadeh, B. Ramezanzadeh, M. Mahdavian, G. Bahlakeh, Development of metal-organic framework (MOF) decorated graphene oxide nanoplatforms for anti-corrosion epoxy coatings, Carbon. 161 (2020) 231–251, https://doi.org/10.1016/j.carbon.2020.01.082.
[44] X. Wang, Y. Li, C. Li, X. Zhang, D. Lin, F. Xu, Y. Zhu, H. Wang, J. Gong, T. Wang, Highly orientated graphene/epoxy coating with exceptional anti-corrosion performance for harsh oxygen environments, Corros. Sci. 176 (2020), 109049, https://doi.org/10.1016/j.corsci.2020.109049.